Crystal Growth Mechanisms of BiFeO 3 Nanoparticles

Xiaofei Bai, Matthieu Bugnet, Carlos Frontera, Pascale Gemeiner, Jérôme Guillot, Damien Lenoble, Infante Ingrid C.

Crystal growth mechanisms of $BiFeO_3$ nanoparticles

Journal:	*Inorganic Chemistry*
Manuscript ID	ic-2019-00461j.R3
Manuscript Type:	Article
Date Submitted by the Author:	n/a
Complete List of Authors:	Bai, Xiaofei; Institut des Nanotechnologies de Lyon, CNRS UMR5270 ECL INSA UCBL CPE Bugnet, Matthieu; MATEIS, CNRS UMR 5510, INSA Lyon, UCBL Lyon 1 Frontera, Carlos; Institut de Ciència de Materials de Barcelona Gemeiner, Pascale; Laboratoire Structures Propriétés et Modélisation des Solides Guillot, Jérôme; Luxembourg Institute of Science and Technology, Materials Research and Technology Department Lenoble, Damien; Luxembourg Institute of Science and Technology, Materials Research and Technology Department Infante, Ingrid; Institut des Nanotechnologies de Lyon, CNRS UMR5270 ECL INSA UCBL CPE

Crystal growth mechanisms of $BiFeO_3$ nanoparticles

*Xiaofei Bai[1,4], Matthieu Bugnet[2], Carlos Frontera[3], Pascale Gemeiner[4], Jérôme Guillot[5], Damien Lenoble[5], Ingrid C. Infante[1]**

1. Institut des Nanotechnologies de Lyon, CNRS UMR5270 ECL INSA UCBL CPE, 69621, Villeurbanne, France

2. Univ Lyon, INSA Lyon, UCBL Lyon 1, MATEIS, UMR 5510 CNRS, 69621 Villeurbanne Cedex, France

3. Institut de Ciència de Materials de Barcelona, ICMAB-CSIC, Campus UAB, Bellaterra E-08193, Spain

4. Laboratoire Structures, Propriétés et Modélisation des Solides (SPMS), CentraleSupélec, CNRS-UMR8580, Université Paris-Saclay, Gif-sur-Yvette, France

5. Luxembourg Institute of Science and Technology, Materials Research and Technology Department, L-4422 Belvaux, Luxembourg

Abstract: A wet-chemical synthesis process was designed to obtain reproducible single-phase multiferroic $BiFeO_3$ nanoparticles. The phase purity, single crystallinity, and size of the nanoparticles are confirmed through the analysis of x-ray diffraction patterns, Raman spectroscopy, and high resolution transmission electron microscopy experiments. Crystal nucleation happens within the amorphous-rich area in multiple seeds, leading to the formation of single crystalline nanoparticles with no preferential faceting. Crystallization mechanisms of $BiFeO_3$ nanoparticles were investigated following the Kissinger-Akahira-Sunose approach, indicating that two crystallization steps are responsible of the complete $BiFeO_3$ nanoparticle formation. The first crystallization step involves a maximum of 70% of the final crystal volume, arises from nanocrystal nucleation and growth. The second step occurs above this threshold crystal volume fraction, and is related to nano-crystallite coalescence process. Analysis of the thermodynamic process of the crystallization of $BiFeO_3$ nanoparticles following Ostwald rules suggest a relatively low energetic barrier for crystal nucleation,

highlighting that phase pure, single crystalline $BiFeO_3$ nanoparticles are obtained using the present optimized wet-chemical synthesis process, with temperatures as low as 450 °C.

INTRODUCTION

Bismuth ferrite (BFO), a promising room temperature multiferroic material, has attracted strong attention because of its relatively low bandgap ($E_g \approx 2.6$-2.8 eV), large ferroelectric polarization and antiferromagnetic order, all coexisting at room temperature (RT), opening the path to the potential control of optical, electrical or magnetic properties using different external stimuli[1]. At RT, BFO crystallizes in rhombohedral *R3c* structure with ferroelectric polarization along the $[111]_R$ direction (T_c = 830 °C), and exhibits an antiferromagnetic G-type order (T_N = 370 °C), together with a spin cycloid arrangement of 62nm-period[1]. Obtaining high quality samples and controlling their size play a significant role to tune and exploit the dimensionality effects in ferroelectric and magnetic properties and the ferroelectric/magnetic potential coupling in these multiferroic materials. Importantly, reduced dimensionality and parameters inherent to the synthesis processes are shown to affect not only the final

multiferroic properties of BFO specimens[2-5], and also the crystalline purity. Indeed, the multiferroic *R3c*-BFO perovskite is thermodynamically in competition with other phases (mostly, $Bi_2Fe_4O_9$ and $Bi_{25}FeO_{40}$)[4, 6]. Different approaches aiming at synthesizing pure *R3c* phase specimens have been explored, using different chelates and employing wet chemical methods[4, 7-9]. A summary of different methods for synthesizing BFO particles and their correspondent secondary phases can be found in the review of Silva *et al*[7]. In view of obtaining parasitic phase-free nanosized BFO particles, wet-chemical processes using low temperature treatments were employed by Selbach *et al*[4], who compared the effect of different chelates. More recently, Ortiz-Quiñonez *et al*[8]. developed an easy method to obtain high purity BFO nanoparticles, using even lower synthesis temperatures than those in previously reported processes. These wet chemical routes to synthesize BFO nanoparticles exploit the transformation from an amorphous phase to a crystalline one, which are dependent on the solvent, chelates and temperature treatment. This process follows different thermodynamic steps, including nano-crystal nucleation, crystal growth and coalescence, which are poorly understood to date for materials containing volatile elements or for those having crystalline phases with similar Gibbs free energy, such as BFO. Deeper knowledge on

the crystallization process can be obtained from calorimetry results analyzed using out of equilibrium models, as the Kissinger-Akahira-Sunose (KAS) one[10-13], to determine the characteristic parameters of the crystallization mechanisms. Finally, combining KAS model analysis with characterization techniques granting the nanoparticle phase nature, homogeneity, size, structure and functional properties, both at the atomic scale and at the microscale, provides a unique opportunity to link nanoparticles crystallization mechanisms and corresponding properties to achieve the final goal of tuning them on demand.

In this work, we present a detailed study on the crystalline growth mechanisms of pure phase BFO nanoparticles, combining experimental evidences of the nanoparticle crystalline quality and thermodynamic analysis. Following a facile wet-chemical method based on sol-gel reaction and calorimetry analysis, we explicitly get information from the synthesis temperature process, and establish the parameters to obtain single crystalline, phase-pure, BFO nanoparticle synthesis conditions. We show that BFO nanoparticles undergo a two-step crystallization process, deduced from a non-isothermal KAS analysis of the calorimetry data. Through studying the nanoparticles crystallization mechanisms, the particle crystallization process can be

consequently controlled. Our study on BFO growth mechanisms highlights the complexity of the crystallization process in these nanoparticles, which is of high importance, and must be considered to widely capture the structure-property relationships.

EXPERIMENTAL SECTION

All chemical reagents were of analytical grade and used without any further purification. In a typical synthesis process, an aqueous solution of 12 mL was first prepared by blending nitric acid (4 mL) in deionized water (8 mL), then $Bi(NO_3)_3{\cdot}5H_2O$ (0.005 mol), $Fe(NO_3)_3{\cdot}9H_2O$ (0.005 mol) were dissolved in the solution while stirring at room temperature. After stirring continuously for 20 min, the solution became clear and light yellow. Then, tartaric acid (TA) (0.01 mol) and ethylene glycol (EG) (0.01 mol) were added to the solution, maintaining the continuous stirring. Finally, the mole ratio of metal ions, TA and EG in the solution was held at $n_{(\mathrm{Bi}^{3+}+\mathrm{Fe}^{3+})}{:}n_{\mathrm{TA}}{:}n_{\mathrm{EG}} = 1{:}1{:}1$, which contributes to the formation of cross-linked structures by esterification between TA and EG, and maintains stoichiometric chelation. Once the reagent in solution was completely dissolved, the mixture was heated up to 80°C via slow temperature ramping

rate (10 °C/h), and stirred continuously to ensure complete cation complexing. The solution displayed a homogeneous yellow colour which deepen gradually with time increasing. Maintained the temperature at 80 ºC until the solvent evaporated completely, while the viscosity increased. Then, the mixture was transferred to the air-blast oven, and kept under 100 °C for 10h. The mixture of uniform viscosity was converted into a dry porous polymeric precursor. This precursor mixture was ground into a fine powder using an agate mortar. Phase-pure BFO nanoparticles were synthesized by calcining the precursor powder in air for 2 h under 450 °C.

Differential scanning calorimetry (DSC) experiments were performed with TG-DSC 92 SETARAM setup using different temperature ramps. Once the temperature range related to the exothermal peaks, identified as the occurrence of the degradation of solvents and chelants, was determined, multiple temperature steps were applied to optimize the sintering process, to keep the chemical stoichiometry, and synthesize pure phase BFO nanoparticles. Crystal phases, structure and phononic fingerprint were determined by x-ray diffraction (XRD) on a Bruker D2 Phaser diffractometer using Cu Kα radiation in theta−theta configuration, and by micro-Raman analysis using a Labram-Horiba spectrometer under He-Ne laser excitation (632.8 nm). XRD data was

typically collected with angular step size of 0.01° and scanning speed of 0.01°/s, 5 sec stop at every step point, to provide enough signal to noise ratio for Rietveld refinement procedures of the unit cell parameters, crystallite size and microstrain (using FullProf suite of programs[14]). A reference LaB6 sample data, measured in the same conditions, were used to determine the diffractometer resolution function. BFO nanoparticles were also characterized by high resolution transmission electron microscopy (HRTEM) using an FEI Titan ETEM, operated at 300 kV, equipped with a Gatan OneView CMOS detector, and a Gatan imaging filter Tridiem 965 ER. An electron energy-loss spectroscopy (EELS) resolution of ~1 eV, and a dispersion of 0.1 eV/channel were used for the acquisition of core-level excitation spectra.

RESULTS AND DISCUSSION

During the synthesis procedure, the use of tartaric acid as cationic chelate captures the different cations by exploiting the chelation of OH-groups with the metallic ions, which is beneficial to obtain the pure phase at low synthesis temperature. Furthermore, ethylene glycol, as an auxiliary solvent, can react with tartaric acid through esterification, which forms a homogeneous network with the metallic ions fixed inside

it. In practice, ethylene glycol has been identified as a suitable solvent to prepare metal oxides (*e.g.* $SrBi_2TaO_9$ and $Ba_{0.5}Sr_{0.5}TiO_3$)[15-16] as a result of the presence of two terminal hydroxyl groups in its molecular structure, which ensure the protection of its heterometallic units during the hydrolysis reaction. Furthermore, it was reported that linear structured molecules, such as ethylene glycol, favour the sol stabilization[17]. Hence, ethylene glycol as a solvent can prevent the hydrolysis of bismuth cation, and keep the stoichiometric ratio of bismuth and iron within the cross-linked network, despite their different electronegativities[18]. This network structure may reduce the energy required for successful dissolution and recrystallization to form pure BFO during the wet-chemical process. In other words, the reaction kinetics of BFO are remarkably accelerated by using ethylene glycol as solvent[18-19]. Thus, the network structure can give rise to homogeneous nucleation by reaction of ethylene glycol with tartaric acid, and it is the precondition for the formation of pure phase BFO[20-23].

Using the precursors previously mentioned, calorimetric and XRD results leading to optimized sintering conditions of BFO nanoparticles are included in Figure 1. Initially, for the precursor sintering process, a one-step thermal process is applied, as shown in Figure 1(b). In this procedure, the precursor is heated up to the synthesis

temperature (450 ºC) at a given ramp (5 ºC/min), kept at this temperature for two hours, then slowly dropped to RT by self-cooling. The corresponding XRD patterns of the final products indicate the presence of parasitic phases, as shown in Figure 1(d). Remarkably, bismuth being a more volatile cation compared to iron within the sintering temperature range, Fe-rich phases, such as $Bi_2Fe_4O_9$, are detected through phase identification in the XRD pattern. This parasitic phase stabilization is attributed to the higher local temperature inducing the evaporation of the volatile Bi-cation[4, 24]. A second approach for the sintering process was to adjust the temperature and time to degrade the solvents and chelants within the precursor powders, and prevent Bi-volatility. DSC experiments were performed as shown in Figure 1(a). Two exothermic peaks appear successively from 200 °C to 350 °C, and no other peaks are detected at higher temperatures. These two exothermic peaks are related to the stepwise decomposition of tartaric acid, ethylene glycol and the network structure created by the esterification. Since the decomposition temperature of tartaric acid and ethylene glycol is close to 200 °C, a great amount of heat exchange for a very short time induces local overheating of the precursor, which promotes the evaporation of Bi, and then leads to

Bi:Fe:O stoichiometry of the final products away from the expected 1:1:3 of the pure perovskite unit cell[24].

In order to avoid non-stoichiometry, a three-step temperature procedure is set (Figure 1(c)) to dissipate the heat-shock that the precursor mixture can experience within the thermal windows of the exothermic transitions. For that, the starting temperature point of each exothermal peak (T_1 and T_2 in figure 1(a): 200 °C and 250 °C) is held for a relatively long time (60 min) and the heating rate from T_1 to T_2 is kept slowly (1 °C/min) on the promise of other temperature parameters identical. This operation prevents the interference from heat-shock for Bi-stoichiometry in the whole synthesis process, and suppresses parasitic phase formation to the utmost extent. The success of the three-step method displayed in Figure 1(c) in preventing parasitic phase formation is confirmed by the XRD pattern shown in Figure 1(e). This pattern is characteristic of pure BFO phase, obtained after sintering of an equivalent precursor mixture as that used with the single step process. Remarkably, pure phase BFO nanoparticles were naturally formed without extra treatment process and free of parasitic phase. We provide evidences of stoichiometry of the pure phase nanoparticles using x-ray photoelectron spectroscopy (XPS) (See Supporting

Information XPS Analysis). A Bi:Fe atomic ratio of approximately 1:1 has been found (18.9:16.2 ≈ 1:1), confirming the expected stoichiometry in BFO nanoparticles synthesized by the three-step temperature process. Furthermore, the XRD pattern of the amorphous phase after sintering at 400°C for 2 hours is shown in Figure S1. It is clear that there is no crystalline phase after annealing below 450°C.

The Rietveld refinement of the XRD patterns of 450°C nanoparticles is shown in Figure 2(a). From the XRD data, BFO nanoparticles belong to the *R3c* space group, and present a mean crystallite size of ~36 nm. The pseudotetragonal normalized lattice parameters a_n and c_n are consistent with values reported elsewhere[25-26]. This means that the polarization, which is directly proportional to the square-root of the distortion[25], can be believed to remain almost unchanged in the studied size (see Table 1). From Rietveld analysis the lattice microstrain is evaluated (isotropic and anisotropic strain values, Table 1), arising from surface imperfection, vacancies and dislocations. In BFO nanoparticles, inhomogeneous strain from local distortions is smaller for larger BFO nanoparticles (corresponding results from nanoparticles synthesized at 600 °C also included in Table 1), where strain relief mechanisms exist[25, 27].

The inset of Figure 2(a) shows the acquired HRTEM image on pure 450°C BFO nanoparticles. It is worth mentioning that the crystalline size deduced from Rietveld refinement of the XRD pattern is in agreement with the nanoparticle size observed by HRTEM. Clear lattice texture is observed, indicating the internal defect-free nature of the sample with high degree of crystallinity. It is worth noting that some amorphous phase surrounds the crystal, which is related to the low synthesis temperature, where precursors cannot be fully transformed into crystal. As deduced from the almost equivalent values of isotropic and anisotropic strain (Table 1), the remaining amorphous phase, which has no preferential site distribution, can be at the origin of the development of micro-strain in the nanoparticles with no particular anisotropy.

The structure of BFO nanoparticles is also studied using micro-Raman spectroscopy at room temperature, as shown in Figure 2(b). The peaks assigned as A1 and E are in agreement with previous calculated and experimental results[28-29] corresponding to the *R3c*-BFO compound. The lower wavenumber vibration modes below 170 cm^{-1} arise from Bi motions, oxygen motions strongly dominate the modes above 267 cm^{-1}, and Fe motions are mainly involved in the modes between 152 and 261 cm^{-1}. Modes higher than 600 cm^{-1} belong to the second-order Raman scattering, and are related to the

electron-phonon interaction in BFO. The mode assignment in BFO nanoparticles (Figure 2(b)) is consistent with reported results[28-29], suggesting that BFO nanoparticles keep the *R3c* space group with no change crystal structure. A detailed list of the different assigned modes can be found in Supporting Information (Figure S5 and Table S3).

To get more insight into the local electronic structure of BFO nanoparticles, EELS measurements at the O *K* and Fe $L_{2,3}$ edges were performed, and are shown in Figure 2(c) and (d), respectively. Overall, the energy-loss near edge structures (ELNES) O *K* and Fe $L_{2,3}$ edges can be qualitatively identified as those of rhombohedral BFO in thin film or bulk forms[30-35]. The ELNES of the O 1*s* excitation has been previously interpreted by multiple scattering calculations for *R3c*-BFO[31, 33]. Fine structure A1 just above the Fermi level (see Figure 2(c)) arises from hybridized O 2*p* – Fe 3*d* states, while fine structure A2 has been interpreted in divergent ways as hybridized O 2*p* – Bi $5d^{82}$, O 2*p* – Bi 6*sp*[35], or O 2*p* – Bi 6*p* – Fe$3d^{83}$ states. The crystal field splitting of the Fe 3*d* states into t_{2g} and e_g symmetry, is contained within peak A1 and not observable with the energy resolution used to acquire the spectra in figure 2(c). Indeed, the crystal field splitting is visible in spectra acquired with higher energy resolution in EELS[31], and

x-ray absorption spectroscopy data[32, 34-35]. At higher energy, fine structure B can be assigned to hybridized O 2*p* – Fe 4*sp*[32-33] with the contribution of Bi *p* and *d* states[33]. While the fine structures are broadened by the energy resolution (~1 eV), the variation of intensity of A_2 relative to A_1, and $A_{1,2}$ relative to B, compared to spectra in the literature can arise from the nanometric size of the particles[32], as well as the different strain state when compared to thin films[30, 34]. The Fe $L_{2,3}$ ELNES, shown in Figure 2(d), exhibits two main features, L_3: Fe $2p_{3/2} \rightarrow$ Fe $3d$ and L_2: Fe $2p_{1/2} \rightarrow$ Fe$3d$, with a spin-orbit splitting of ~13.0 eV, in agreement with previously reported values in the literature for BFO nanoparticles[31]. The t_{2g}-e_g crystal field splitting can be identified from the small shoulder (t_{2g}) at the L_3 edge onset (see arrow). Similarly, two distinct features can be observed at the L_2 edge (see arrow). The more intense L_2 e_g compared to the L_2 t_{2g}, also confirms the agreement with rhombohedral BFO[31, 35].

The FFT of different area of the nanoparticles, as shown in Figure 3(d)-(e), have equivalent diffraction spots, indicating that the individual nanoparticles can be considered as single crystals (FFT of different area of other nanoparticles are shown in Figure S1). The FFT patterns are indexed with spots corresponding to (012) and (104) planes of the Hexagonal lattice, which correspond to d-spacing values in

agreement with those deduced from XRD Rietveld refinement analysis (details on these values are included in the Supporting Information Table S1, Table S2 and Figure S4). The amorphous phase is visible at the surface of nanoparticles, as seen in the inset of Figure 2(a), and also in other areas further away from the nanoparticle (Figure 3(a), solid-line square). Remarkably, when the precursor solution is prepared, the heating leads to the formation of a gel, at higher temperature than the gel temperature itself, the pyrolysis process thus creates an amorphous metal-oxygen network[36]. The final crystallization takes place under continuous heating at relatively low temperature (450 °C), thus becoming rather difficult to obtain the amorphous phase completely pyrolyzed. The intermediate products, between amorphous metal-oxygen bond structure and the final crystallite, are consequently found within the final products together with the BFO nanoparticles. Lattice fringes are detected in ~5 nm large nano-crystallites, as shown in Figure 3(b, c) and Figure S2(b). The presence of these nano-crystallites embedded in an amorphous matrix could be an intermediate phase leading to BFO nanoparticle crystallization. To get more information on the details of the process leading to the BFO crystalline phase formation, we have performed calorimetry experiments.

Differential scanning calorimetry (DSC) measurements were carried out using BFO precursors in order to determine the crystallization parameters leading to the formation of BFO nanoparticles. The non-isothermal crystallization kinetics of Bi-Fe-O amorphous were investigated using different heating ramps on the same precursors, leading to different thermodynamic processes, as depicted in Figure 4. In Figure 4(a), the DSC curves of Bi-Fe-O amorphous crystallization exhibits two exothermic peaks above 450 °C, and these peaks are shifted to higher temperature with increasing heating rate due to thermodynamic effect. To determine the origin of the DSC peaks, we investigated the size, morphology and crystallinity of nanoparticles synthesized at low temperatures (450 °C) and compared these results with those obtained on nanoparticles synthesized at high temperature (600 °C). The case samples studied here would help us investigating BFO nanoparticles at the early stages of crystallization, since their synthesis temperature corresponds either to that of the onset (450 °C) of the observed exothermic peaks, or to a temperature (600 °C) well above them. Macroscopic XRD-experiments corresponding to nanoparticles synthesized at 450 °C (Figure 2(a)) and 600 °C (Supporting Information, Figure S2) are used to determine the structure parameters, and are summarized in Table 1 (particle size

obtained from scanning electron microscopy, not shown here). The XRD patterns of all nanoparticles correspond to pure phase *R3c* $BiFeO_3$. We note that very close values of crystal and nanoparticle sizes are observed for nanoparticles synthesized at 450 °C (36 nm), whereas nanoparticles synthesized at 600 °C are larger (190 nm) than their crystal size (94 nm) (Table 1). These results suggest that 450 °C nanoparticles can be considered as single crystal nanoparticles whereas 600 °C ones are polycrystalline ones. Besides, for the first stages of crystallization, the HRTEM images on nanoparticles synthesized at 450 °C (Figure 3(a)) revealed the existence of BFO single crystal nanoparticles, coexisting with remaining amorphous matrix. From these results, we conclude that the DSC exothermic peaks can be attributed to different processes: the low temperature exothermic peak should capture the nanocrystal nucleation and growth processes, leading to the observed single crystal nanoparticles, and the high temperature exothermic peak arises from the single crystal nanoparticle coalescence, leading to polycrystalline nanoparticles as final product.

The whole crystallization scenario can be summarized to the following: nano-crystallites of reduced size surrounded by the amorphous matrix appear in large number at the early stages of crystal nucleation. The crystallization of the remaining

amorphous matrix continues at the surface of some of these nano-crystallites, leading to single crystal nanoparticle growth. Thus, single crystal BFO nanoparticles coexist with part of the amorphous matrix at this stage. On the other hand, at higher synthesis temperature, the process of nano-crystallite growth is no longer favorable against merging of individual nano-crystallites into larger polycrystalline nanoparticles, formed from coalescence of individual nano-crystallites.

According to the morphology observed in Figure 3(a), the synthesis process of BFO nanoparticle process is sketched in Figure 5. It can be seen that the esterification reaction (see Supporting Information Sol-gel process) occurs under heating at 80°C during the 2nd step of the heating process. When the precursor decomposition temperature is attained at the 3rd step of that process, the metal-oxygen bond structure exists in an amorphous phase, which is shown in 4th step. Further heating up to 450°C, the nucleation of nanocrystals is more favorable than the disordered metal-oxygen bond structure, the energy barrier for this formation is overcome by thermal fluctuations. Thus, the crystal nuclei start to appear in 5th step of the heating process. The following process consist of the coalescence of nanocrystals and continuous

crystallization of the remaining amorphous phase, which are indicated in 6th step. This process is avoided if the final annealing temperature is set below 450 ºC.

The crystallization difficulty or energetic barrier is evaluated by the apparent activation energy E_a within different crystallization kinetics models. On the basis of the dynamic DSC measurements for different heating rate, the Kissinger-Akahira-Sunose (KAS) model enables the determination of the individual apparent activation $E_a(x)$ values[37], at each step of the crystallization process, indicated by the crystallized volume fraction values x, and over a wide range of x, according to equation[38-39]

$$\ln\left(\frac{\beta}{T_x^2}\right) = \ln\left(\frac{AR}{E_a(x)}\right) - \frac{E_a(x)}{RT_x}, \quad (1)$$

where T_x is the temperature that the crystallised fraction reaches x, β stands for the heating rate, R is the gas constant, A is a kinetic parameter. As a consequence of the thermodynamic effects, leading to a difference in the crystallization ratio as a function of the heating rate, T_x depends on the heating rate β. Inspecting equation (1), the left side term $\ln\left(\frac{\beta}{T_x^2}\right)$ linearly depends on the inverse temperature $1/T_x$, and the second term of the right side of the KAS equation as well. Thus, the apparent activation energy $E_a(x)$ can be evaluated just from this terms for the whole x range by a linear fit (details are included in the Supporting Information Figure S6). The dependence of the local values

of activation energy $E_a(x)$ on the crystallization volume fraction x is illustrated in Figure 6. In the initial stages, the higher values of $E_a(x)$ suggest a high-energy barrier for crystallization, the large initial slope determined from $E_a(x)$ vs x indicates that the first crystallization steps allow to go beyond a crystallization threshold, representing a very reduced amount in volume fraction of the overall precursors ($dE_a(x)/dx$ is shown in the Supporting Information Figure S7 (c)). Once the crystallization is initiated, the activation energy $E_a(x)$ begins to drop off until ~70% of crystallization fraction, then upwards again. Furthermore, the apparent activation energy $E_a(x)$ having a minimum at ~70% indicates that the crystallization reaction becomes easier when the crystalline fraction is close to this value. Figures 4(b)-(e) show the Gaussian fitted exothermal peaks for different heating rate. As explained above, the first peak is related to crystal nucleation and growth, the second one arises from the coalescence process. The shaded areas represent the 70% crystallization fraction for different heating rates. For the 10 °C/min heating rate DSC curve, the corresponding 70% crystallization area is essentially dominated by the nucleation and growth peaks, with no major contribution of the crystal coalescence process. For DSC experiments with higher heating rates, the corresponding peaks have larger temperature spreading and they are centered on

temperature values closer one to another. Thus, a higher correlation between nucleation, crystal growth and coalescence exists for the largest heating rates (the two peaks evolution vs heating rate are shown in Supporting Information Figure S7 (a) and (b)). From the minimum effective barrier height observed at ~70% of crystallized volume fraction, this percentage is deduced to set the boundary between nucleation, growth and coalescence mechanisms of these nanoparticles following the present synthesis process. Above ~70% of crystallized volume fraction, the effective activation energy E_a increases (Figure 6).

Such behavior can be explained from the wider picture of the whole crystallization process based on thermodynamic arguments and considering that the activation energy during the crystallization process is not a constant, which is consistent with Ostwald rule[40]. In the initial stage of crystallization, the activation energy is expected to be the highest and energy barrier can be overcome by thermal fluctuation, leading to a fast transition via atomic displacement. Based on non-equilibrium thermodynamics, the Ostwald's step rule minimizes the entropy in this initial transformations process[41]. Crystallization often starts in such a way that a thermodynamically unstable phase appears first followed by recrystallization to

thermodynamically stable phase[40]. From a thermodynamic point of view, it is worth noting that the process from nucleation to growth is transient and strongly overlapping within the temperature range and ramp conditions used in the synthesis process. Taking into account these thermodynamics constraints, the first stages of the nanoparticle crystallization are described as independent nucleation processes followed by crystalline growth immediately[4], which are accompanied by a decrease of the system disorder. This crystallization process is related to the intermediate crystalline phase formation from an amorphous solid (Figure 3(b)) accompanied by an activation energy reduction. Few studies report the detailed chemical stability of amorphous and crystalline phases of BFO, and essentially focus on the comparison between different crystalline phases of Bi oxides, Fe oxides, or Bi-Fe oxides nanoparticles[42] or thin films[43], rather than between the stability of amorphous *vs* crystalline phases of BFO precursors. Although it is not possible to disentangle the contributions of the amorphous and crystalline particle formation energies to the measured enthalpy change, an amorphous to crystalline phase transformation is intrinsically related to a reduction of disorder, thus coupling to entropy changes. This phase transformation can be responsible of the activation energy E_a decrease, leading

to the crystallization of up to 70% of the volume into crystals (nucleation and growth process), the formation of energetically stable nano-crystallites that have overcome the energy barrier along with their subsequent coalescence are favorable for further transition at high temperature. Above concentration ~70%, the increase of activation energy E_a contributed from the surface energy of nano-crystallites, which should be taken into account the coalescence process. We note that the surface chemical potentials in perovskite oxides are typically larger than the bulk counterparts[44-45]. The increase in E_a for crystalline volume fraction larger than ~70% can account for the crystal growth mechanisms that are related to the number of available crystalline particles as well as to their mutual interaction, which is based on particle rotation induced particle coalescence mechanism. In addition, from DSC analysis, we note that the integral intensity of the first exothermic peak is larger than that of the second one. This result can be explained by a larger energy barrier for nucleation and growth (lower temperature peak) than for coalescence (higher temperature peak), which supports the results shown with Figure 6. The variation of $E_a(x)$ can thus be attributed to the crystal nucleation, growth and coalescence in the crystallization process. The present results and analysis highlight that the combination of all afore-mentioned processes,

leading to particle transformations from single nanocrystal into grown (coalescent) nanocrystals, can promote the activation energy E_a to increase for crystallization fractions above 70% based on the previously explained surface energy arguments.

CONCLUSIONS

In summary, single crystal BFO nanoparticles are synthesized via wet chemical method under elaborate temperature process. The optimized chelation for pure phase is discussed, which indicated that tartaric acid and ethylene glycol are the optimal combination pure phase BFO. HRTEM images reveals that the BFO nanoparticles are single crystalline, and that the average crystal size is around 36 nm, in agreement with Rietveld refinement analysis of the XRD patterns. The nanoparticles crystalline growth mechanisms are studied by DSC using a Kissinger-Akahira-Sunose model of non-isothermal transformations. The local activation energy $E_a(x)$ are calculated to illustrate that in the range of 0-70% crystallization fraction, the crystallization process is dominated by nucleation and growth process. Above 70%, the crystallization process is consistent with a nano-crystallite growth via coalescence dominated by the reduction of surface energy. These findings suggest that controlling the process temperature and

employing appropriate chelates are key factors to obtain pure phase nanoparticles, especially oxides containing volatile elements such as Bi, Pb, *etc*.

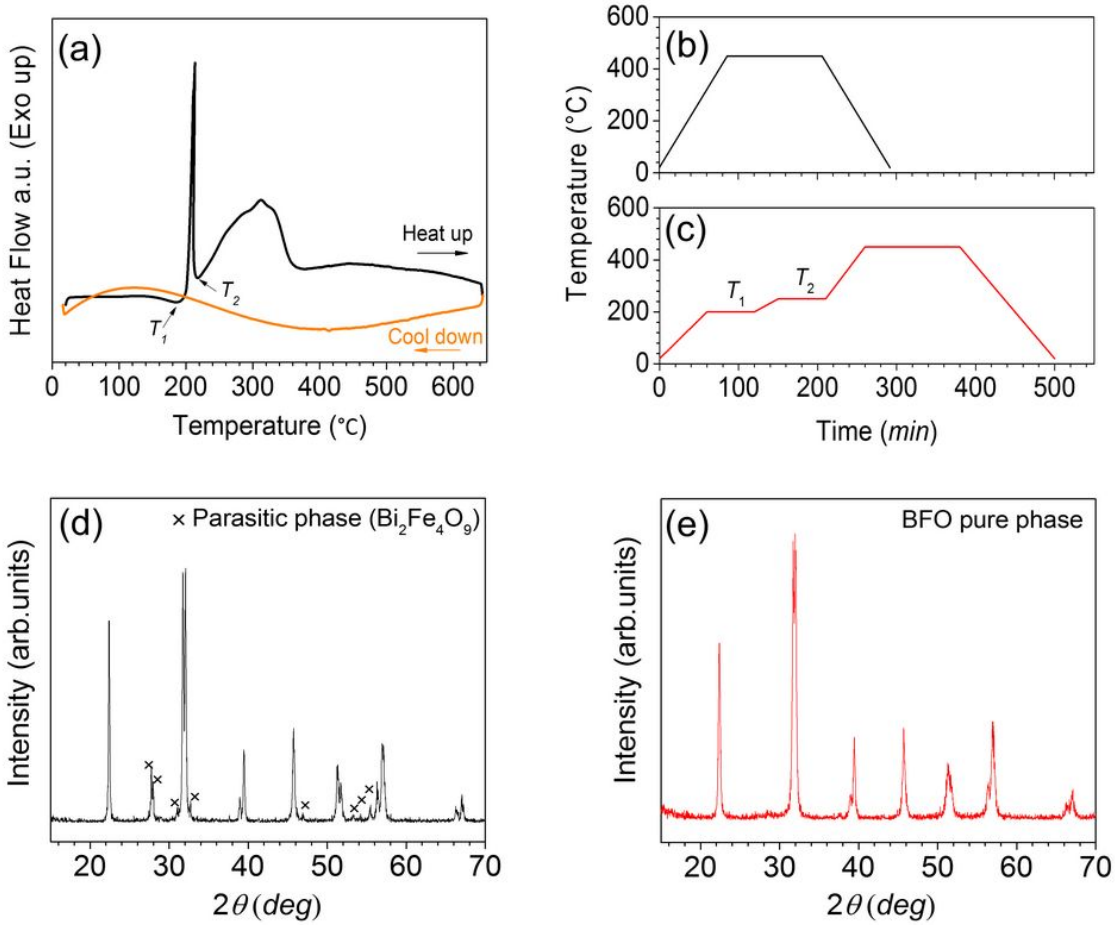

Figure 1. (a) Heating and cooling ramps of DSC experiments using BFO precursor powders. In (b) and (c), the different heating processes for BFO nanoparticles synthesis are depicted, being (b) the single step one and (c) the three step one. In (d) and (e), XRD patterns of nano BFO synthesized by (d) the single step heating process shown in (b), and by (e) the three step heating process shown in (c). The peaks identified with cross symbols shown in (d) arise from parasitic phases.

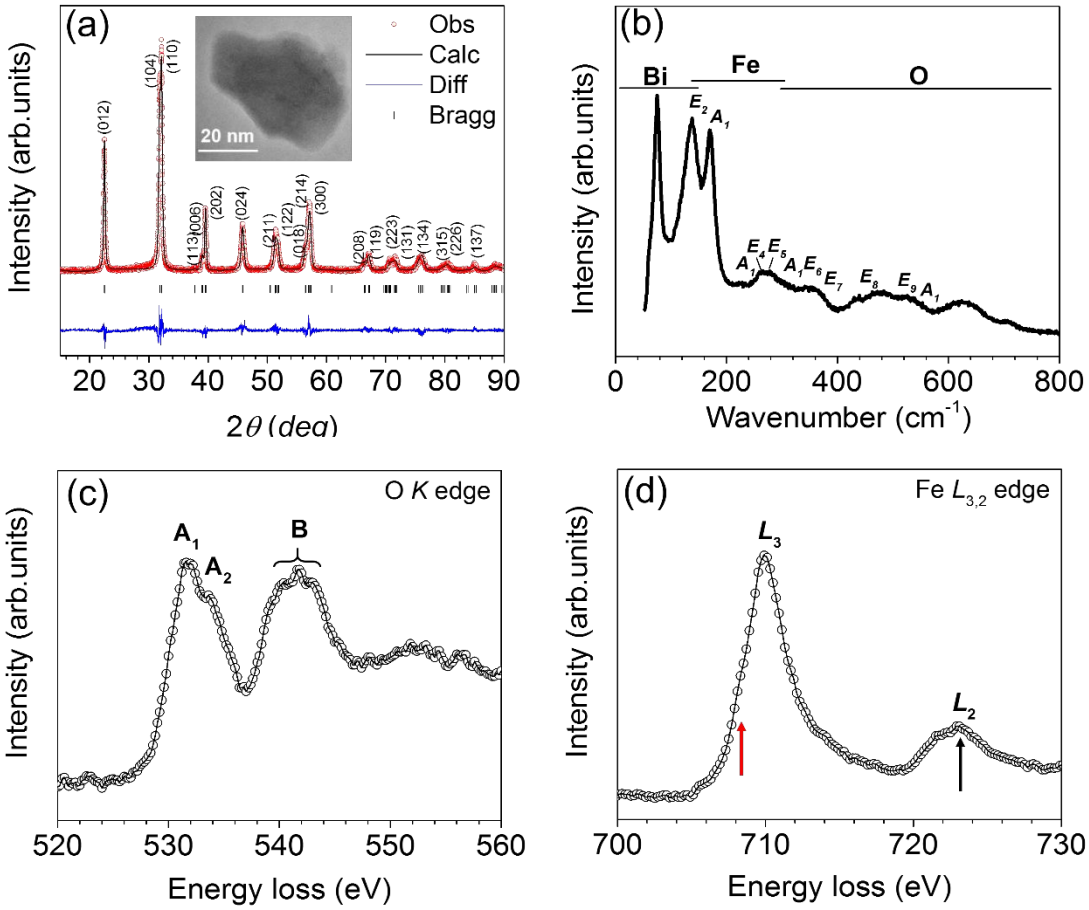

Figure 2. (a) X-ray diffraction data (symbols) and corresponding Rietveld refinement (lines) of BFO nanoparticles. Inset: a characteristic BFO nanoparticle observed by HRTEM, scale bar of 20 nm. (b) Raman spectrum of BFO nanoparticles, *E* modes and A_1 modes are indicated and the corresponding spectrum range arising from phonons primarily related to Bi, Fe or O ions. In (c) and (d), EELS spectra from BFO nanoparticles: (c) O *K* edge spectrum indicating A_1, A_2, and B peaks, and (d) Fe $L_{3,2}$-edge spectrum indicating the corresponding L_3 and L_2 edge position. For more details in the analysis, see the text.

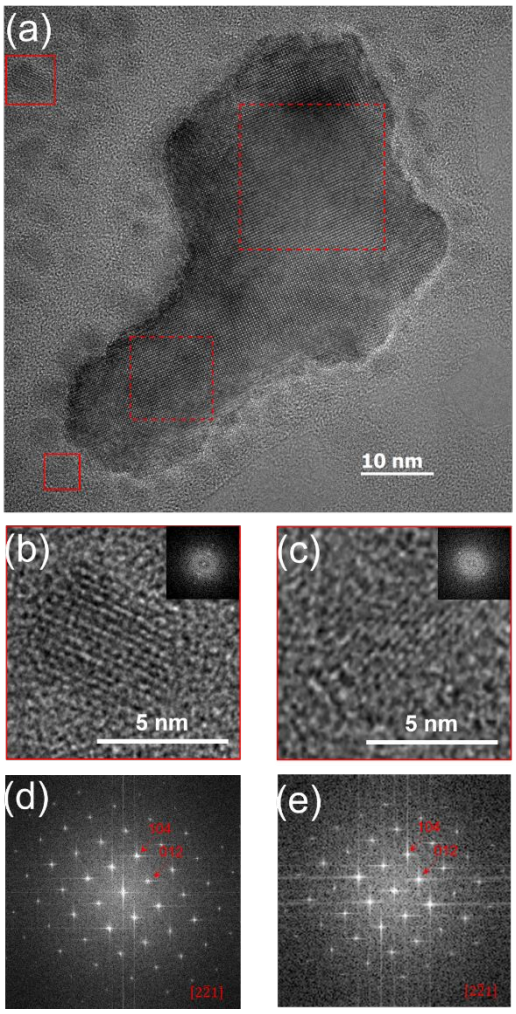

Figure 3. HRTEM images capturing the different formation steps of the BFO nanoparticle crystallization and corresponding analysis. In the central area of the image, to a representative nanoparticle surrounded by nanocrystals. The zoom in a nanocrystal captured within an amorphous rich area region located at the top left corner and left bottom indicated by the solid-line square is shown in (b) and (c), the insets shows the corresponding magnified FFT respectively. The FFTs shown in (d) and (e)

correspond to different areas within the same nanoparticle, indicated by the dashed line squares, (d) from the large square area and (e) from the small square area.

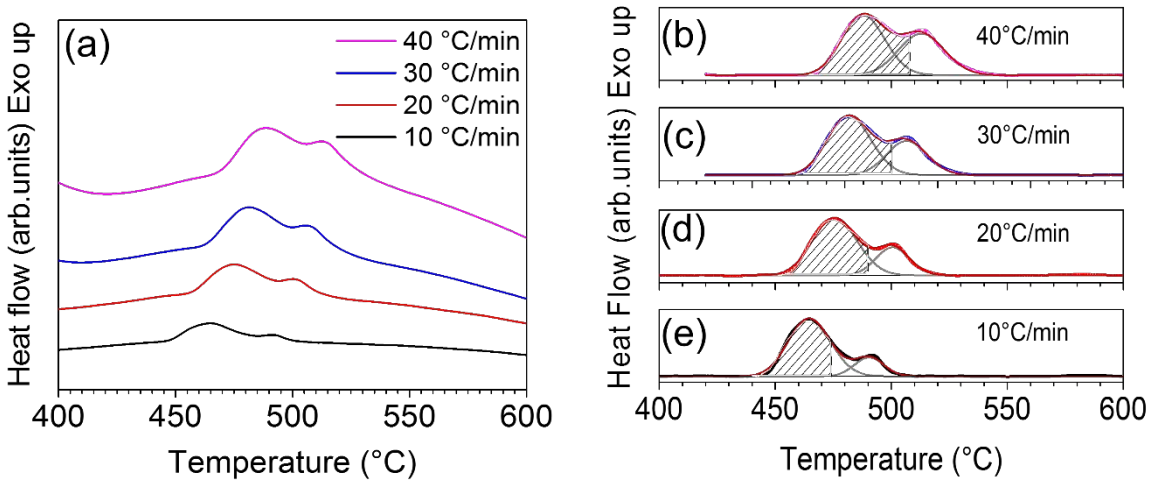

Figure 4. Study of the crystallization of BFO nanoparticles from DSC data collected at different heating rates on the same amorphous powder. (a) Detail of the raw DSC data collected around the crystallization thermal window of the amorphous powder (b-e) Gaussian fitted exothermal peaks related to nucleation and growth, the shaded areas denote the achievement of 70% volume crystallization (base-lines have been subtracted from DSC curves).

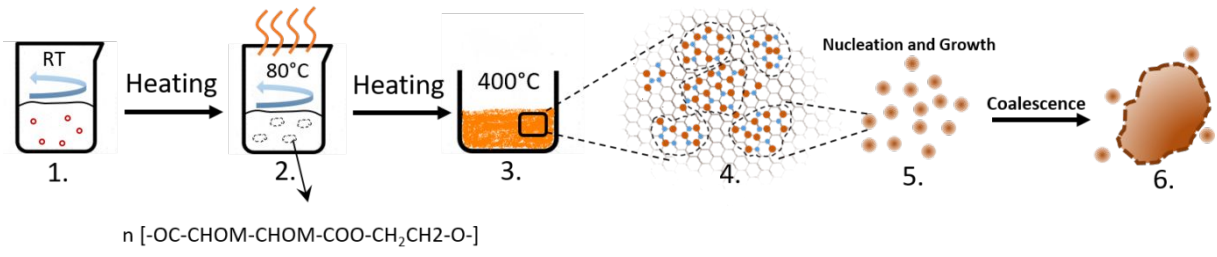

Figure 5. Sketch of the BFO nanoparticle crystallization process following the present sol-gel method.

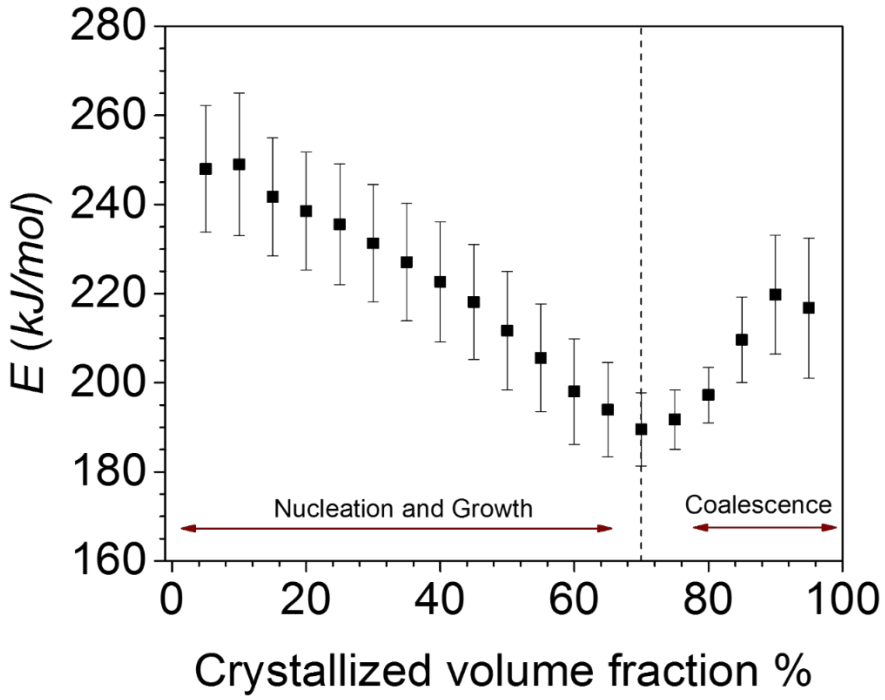

Figure 6. Dependence of local activation energy $E_a(x)$ (by KAS model) on the degree of crystallized volume fraction x.

Table 1. BFO nanoparticles synthesis temperature and corresponding values of particle size, crystallite size, normalized lattice parameters (a_n and c_n)[25] , isotropic and anisotropic strain values.

Synthesis temperature (°C)	Particle size (nm)	Crystalline size (nm)	a_n(Å)	c_n(Å)	Isotropic strain (x10^{-4})	Anisotropic strain (x10^{-4})
450	36	36	3.9457	4.0034	36.8	36.5
600	184	94	3.9449	4.0040	15.0	17.7

AUTHOR INFORMATION

Corresponding Author

ingrid.canero-infante@insa-lyon.fr

Notes

The authors declare no competing financial interest.

ACKNOWLEDGMENT

This work was supported by the IDEXLYON (ANR-16-IDEX-0005) FERLIGHT project from the Université de Lyon. J. G., D.L. and I.C.I. thank the FNR funding provided by the INTER/Mobility FOXCAT project No. 15/9887562. We thank Nagy Valanoor for fruitful discussions.

ASSOCIATED CONTENT

Supporting Information

The Supporting Information (X-ray diffraction studies of the amorphous phase after 2h 400°C sintering and of the 600°C crystalline phase (and corresponding Rietvield refinement), additional high resolution transmission electron microscopy images and corrresponding analysis, details on the Raman spectroscopy analysis, methods for fitting the differential scanning calorimetry data to results with the used KAS kinetic model, explaination of the sol-gel process, X-ray photoelectron spectroscopy analysis) is available free of charge on the ACS Publications website at DOI: http://pubs.acs.org.

REFERENCES

1. Catalan, G.; Scott, J. F., Physics and applications of bismuth ferrite. *Advanced Materials* **2009,** *21* (24), 2463-2485.

2. Wang, J.; Neaton, J.; Zheng, H.; Nagarajan, V.; Ogale, S.; Liu, B.; Viehland, D.; Vaithyanathan, V.; Schlom, D.; Waghmare, U., Epitaxial $BiFeO_3$ multiferroic thin film heterostructures. *science* **2003,** *299* (5613), 1719-1722.

3. Park, T.-J.; Mao, Y.; Wong, S. S., Synthesis and characterization of multiferroic $BiFeO_3$ nanotubes. *Chemical Communications* **2004,** (23), 2708-2709.

4. M., S. S.; Mari-Ann, E.; Thomas, T.; Tor, G., Synthesis of $BiFeO_3$ by Wet Chemical Methods. *Journal of the American Ceramic Society* **2007,** *90* (11), 3430-3434.

5. Infante, I. C.; Lisenkov, S.; Dupé, B.; Bibes, M.; Fusil, S.; Jacquet, E.; Geneste, G.; Petit, S.; Courtial, A.; Juraszek, J.; Bellaiche, L.; Barthélémy, A.; Dkhil, B., Bridging Multiferroic Phase Transitions by Epitaxial Strain in $BiFeO_3$. *Physical Review Letters* **2010,** *105* (5), 057601.

6. Rojac, T.; Bencan, A.; Malic, B.; Tutuncu, G.; Jones, J. L.; Daniels, J. E.; Damjanovic, D., $BiFeO_3$ ceramics: processing, electrical, and electromechanical properties. *Journal of the American Ceramic Society* **2014,** *97* (7), 1993-2011.

7. Silva, J.; Reyes, A.; Esparza, H.; Camacho, H.; Fuentes, L., $BiFeO_3$: a review on synthesis, doping and crystal structure. *Integrated Ferroelectrics* **2011,** *126* (1), 47-59.

8. Ortiz-Quiñonez, J. L.; Díaz, D.; Zumeta-Dubé, I.; Arriola-Santamaría, H.; Betancourt, I.; Santiago-Jacinto, P.; Nava-Etzana, N., Easy synthesis of high-purity $BiFeO_3$ nanoparticles: new insights derived from the structural, optical, and magnetic characterization. *Inorganic chemistry* **2013,** *52* (18), 10306-10317.

9. Zhang, Q.; Sando, D.; Nagarajan, V., Chemical route derived bismuth ferrite thin films and nanomaterials. *Journal of Materials Chemistry C* **2016,** *4* (19), 4092-4124.

10. Kong, L.; Gao, Y.; Song, T.; Wang, G.; Zhai, Q., Non-isothermal crystallization kinetics of FeZrB amorphous alloy. *Thermochimica acta* **2011,** *522* (1-2), 166-172.

11. Joraid, A. A.; Abu-Sehly, A. A.; El-Oyoun, M. A.; Alamri, S. N., Nonisothermal crystallization kinetics of amorphous $Te_{51.3}As_{45.7}Cu_3$. *Thermochimica Acta* **2008,** *470* (1), 98-104.

12. Kuo, C.-W.; Lee, Y.-H.; Hung, I. M.; Wang, M.-C.; Wen, S.-B.; Fung, K.-Z.; Shih, C.-J., Crystallization kinetics and growth mechanism of 8mol% yttria-stabilized zirconia (8YSZ) nano-powders prepared by a sol–gel process. *Journal of Alloys and Compounds* **2008,** *453* (1), 470-475.

13. Malek, T. J.; Chaki, S. H.; Deshpande, M., Structural, morphological, optical, thermal and magnetic study of mackinawite FeS nanoparticles synthesized by wet chemical reduction technique. *Physica B: Condensed Matter* **2018,** *546*, 59-66.

14. Rodríguez-Carvajal, J., Recent advances in magnetic structure determination by neutron powder diffraction. *Physica B: Condensed Matter* **1993,** *192* (1), 55-69.

15. Kao, C.-F.; Yang, W.-D., Preparation of barium strontium titanate powder from citrate precursor. *Applied Organometallic Chemistry* **1999,** *13* (5), 383-397.

16. Wang, W.; Zhou, Y.; Chen, S.; Ye, F.; Jia, D., Preparation of strontium bismuth tantalum (SBT) fine powder by sol-gel process using bismuth subnitrate as bismuth source. *Journal of Materials Science & Technology* **2001,** *17* (1), 25-26.

17. Harris, J. M., *Poly (ethylene glycol) chemistry: biotechnical and biomedical applications*. Springer Science & Business Media: 2013.

18. Popa, M.; Crespo, D.; Calderon‐Moreno, J. M.; Preda, S.; Fruth, V., Synthesis and structural characterization of single‐phase $BiFeO_3$ powders from a polymeric precursor. *Journal of the American Ceramic Society* **2007,** *90* (9), 2723-2727.

19. Gonzalez, A.; Simões, A.; Cavalcante, L.; Longo, E.; Varela, J. A.; Riccardi, C., Soft chemical deposition of $BiFeO_3$ multiferroic thin films. *Applied physics letters* **2007,** *90* (5), 052906.

20. Liu, T.; Xu, Y.; Feng, S.; Zhao, J., A facile route to the synthesis of $BiFeO_3$ at low temperature. *Journal of the American Ceramic Society* **2011,** *94* (9), 3060-3063.

21. Wang, X.; Lin, Y.; Zhang, Z.; Bian, J., Photocatalytic activities of multiferroic bismuth ferrite nanoparticles prepared by glycol-based sol–gel process. *Journal of sol-gel science and technology* **2011,** *60* (1), 1.

22. Dhir, G.; Lotey, G. S.; Uniyal, P.; Verma, N., Size-dependent magnetic and dielectric properties of Tb-doped $BiFeO_3$ nanoparticles. *Journal of Materials Science: Materials in Electronics* **2013,** *24* (11), 4386-4392.

23. Park, T.-J.; Papaefthymiou, G. C.; Viescas, A. J.; Moodenbaugh, A. R.; Wong, S. S., Size-dependent magnetic properties of single-crystalline multiferroic $BiFeO_3$ nanoparticles. *Nano letters* **2007,** *7* (3), 766-772.

24. Hardy, A.; Gielis, S.; Van den Rul, H.; D'Haen, J.; Van Bael, M.; Mullens, J., Effects of precursor chemistry and thermal treatment conditions on obtaining phase pure bismuth ferrite from aqueous gel precursors. *Journal of the European Ceramic Society* **2009,** *29* (14), 3007-3013.

25. Bai, X.; Wei, J.; Tian, B.; Liu, Y.; Reiss, T.; Guiblin, N.; Gemeiner, P.; Dkhil, B.; C. Infante, I., Size effect on optical and photocatalytic properties in $BiFeO_3$ nanoparticles. *The Journal of Physical Chemistry C* **2016,** *120* (7), 3595-3601.

26. Selbach, S. M.; Tybell, T.; Einarsrud, M.-A.; Grande, T., Size-dependent properties of multiferroic $BiFeO_3$ nanoparticles. *Chemistry of Materials* **2007,** *19* (26), 6478-6484.

27. Mocherla, P. S.; Karthik, C.; Ubic, R.; Ramachandra Rao, M.; Sudakar, C., Tunable bandgap in $BiFeO_3$ nanoparticles: the role of microstrain and oxygen defects. *Applied Physics Letters* **2013,** *103* (2), 022910.

28. Hermet, P.; Goffinet, M.; Kreisel, J.; Ghosez, P., Raman and infrared spectra of multiferroic bismuth ferrite from first principles. *Physical Review B* **2007,** *75* (22), 220102.

29. Haumont, R.; Kreisel, J.; Bouvier, P.; Hippert, F., Phonon anomalies and the ferroelectric phase transition in multiferroic $BiFeO_3$. *Physical Review B* **2006,** *73* (13), 132101.

30. Pailloux, F.; Couillard, M.; Fusil, S.; Bruno, F.; Saidi, W.; Garcia, V.; Carrétéro, C.; Jacquet, E.; Bibes, M.; Barthélémy, A., Atomic structure and microstructures of supertetragonal multiferroic $BiFeO_3$ thin films. *Physical Review B* **2014,** *89* (10),

104106.

31. Rossell, M.; Erni, R.; Prange, M. P.; Idrobo, J.-C.; Luo, W.; Zeches, R.; Pantelides, S. T.; Ramesh, R., Atomic structure of highly strained $BiFeO_3$ thin films. *Physical review letters* **2012,** *108* (4), 047601.

32. Park, T.-J.; Sambasivan, S.; Fischer, D. A.; Yoon, W.-S.; Misewich, J. A.; Wong, S. S., Electronic structure and chemistry of iron-based metal oxide nanostructured materials: a NEXAFS investigation of $BiFeO_3$, $Bi_2Fe_4O_9$, α-Fe_2O_3, γ-Fe_2O_3, and Fe/Fe_3O_4. *The Journal of Physical Chemistry C* **2008,** *112* (28), 10359-10369.

33. Sæterli, R.; Selbach, S. M.; Ravindran, P.; Grande, T.; Holmestad, R., Electronic structure of multiferroic $BiFeO_3$ and related compounds: Electron energy loss spectroscopy and density functional study. *Physical Review B* **2010,** *82* (6), 064102.

34. Borisevich, A. Y.; Eliseev, E.; Morozovska, A.; Cheng, C.-J.; Lin, J.-Y.; Chu, Y.-H.; Kan, D.; Takeuchi, I.; Nagarajan, V.; Kalinin, S. V., Atomic-scale evolution of modulated phases at the ferroelectric–antiferroelectric morphotropic phase boundary controlled by flexoelectric interaction. *Nature communications* **2012,** *3*, 775.

35. Higuchi, T.; Liu, Y.-S.; Yao, P.; Glans, P.-A.; Guo, J.; Chang, C.; Wu, Z.; Sakamoto, W.; Itoh, N.; Shimura, T., Electronic structure of multiferroic $BiFeO_3$ by resonant soft x-ray emission spectroscopy. *Physical Review B* **2008,** *78* (8), 085106.

36. Brinker, C. J.; Scherer, G. W., *Sol-gel science: the physics and chemistry of sol-gel processing*. Academic press: 2013.

37. Leroy, V.; Cancellieri, D.; Leoni, E.; Rossi, J.-L., Kinetic study of forest fuels by TGA: model-free kinetic approach for the prediction of phenomena. *Thermochimica*

Acta **2010,** *497* (1-2), 1-6.

38. Rong, J.; Yang, K.; Zhuang, Y.; Zhong, X.; Zhao, H.; Ni, J.; Tao, S.; Wang, L.; Ding, C., Non‐isothermal crystallization kinetics of Al_2O_3‐YAG amorphous ceramic coating deposited via plasma spraying. *Journal of the American Ceramic Society* **2018,** *101* (7), 2888-2900.

39. Šesták, J.; Simon, P., *Thermal analysis of micro, nano-and non-crystalline materials: transformation, crystallization, kinetics and thermodynamics*. Springer Science & Business Media: 2012; Vol. 9.

40. Chung, S.-Y.; Kim, Y.-M.; Kim, J.-G.; Kim, Y.-J., Multiphase transformation and Ostwald's rule of stages during crystallization of a metal phosphate. *Nature Physics* **2009,** *5* (1), 68.

41. Nývlt, J., The Ostwald rule of stages. *Crystal Research and Technology* **1995,** *30* (4), 443-449.

42. Selbach, S. M.; Einarsrud, M.-A.; Grande, T., On the thermodynamic stability of $BiFeO_3$. *Chemistry of Materials* **2008,** *21* (1), 169-173.

43. Mei, Z., First-principles Thermodynamics of Phase Transition: from Metal to Oxide. **2011**.

44. Carrasco, J.; Illas, F.; Lopez, N.; Kotomin, E. A.; Zhukovskii, Y. F.; Evarestov, R. A.; Mastrikov, Y. A.; Piskunov, S.; Maier, J., First-principles calculations of the atomic and electronic structure of *F* centers in the bulk and on the (001) surface of $SrTiO_3$. *Physical Review B* **2006,** *73* (6), 064106.

45. Heifets, E.; Eglitis, R. I.; Kotomin, E. A.; Maier, J.; Borstel, G., Ab initio modeling

of surface structure for $SrTiO_3$ perovskite crystals. *Physical Review B* **2001,** *64* (23), 235417.

TABLE OF CONTENTS

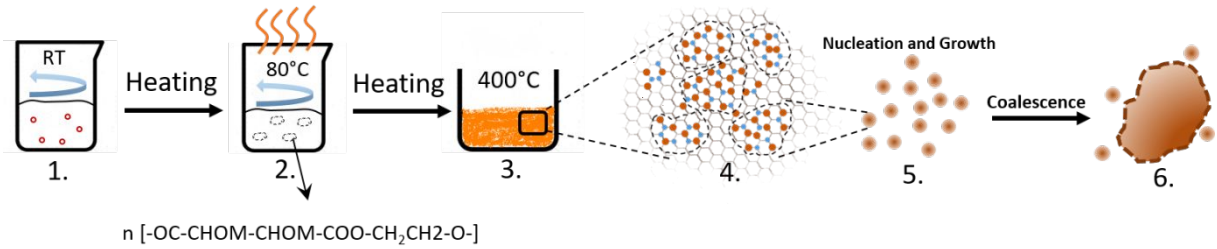

n [-OC-CHOM-CHOM-COO-CH_2CH2-O-]

SYNOPSIS

$BiFeO_3$ nanoparticles have been successfully synthesized via an optimized two-step wet chemical method. Based on a thermodynamic analysis, the initial stages of nanoparticle formation, related to nucleation and growth are investigated. The activation energy for $BiFeO_3$ crystallization as a function of the crystallized volume fraction was determined via Kissinger-Akahira-Sunose model, which shows a threshold value of 70% volume fraction as the limit between nucleation and growth against coalescence.